J. Eur. Opt. Society-Rapid Publ. 2024, **20**, 26

https://doi.org/10.1051/jeos/2024025
Available online at: https://jeos.edpsciences.org

Journal of the European Optical Society-Rapid Publications

RESEARCH ARTICLE OPEN ACCESS

A method of fluorescence molecular tomographic reconstruction via the second-order sensitivity matrix

Wei Zou* and Jiajun Wang

School of Electronic and Information Engineering, Soochow University, Suzhou 215006, China

Received 6 January 2024 / Accepted 5 May 2024

Abstract. Fluorescence molecular tomographic (FMT) reconstruction is commonly solved based on the Jacobian matrix, which is a first-order sensitivity matrix. Basically, using the second-order derivatives for iterative reconstruction can help improve the performance of convergence. In this paper, a reconstruction method of FMT based on the reduction of the second-order sensitivity matrix is proposed. In addition, the strategy of detectors rotation is combined into the inverse reconstruction to further improve the reconstruction quality. The reconstructed results demonstrate that the proposed method accelerates the reconstruction with high precision of inverse solutions.

Keywords: Optics, Fluorescence, Sensitivity matrix.

1 Introduction

Biomedical imaging has gained a lot of attention due to the potential applications for clinical diagnosis and assessment of treatment. This technique can image the physical properties inside an object with measurements taken from around the object [1, 2]. More specifically, fluorescent molecular tomography (FMT) is an important optical imaging modality. The use of fluorescent agents in imaging diseased tissue has the potential for high specificity and contrast. Due to the advantages of safety, low cost, high sensitivity, and reliability, FMT has the important preclinical and clinical applications as pharmacokinetics. FMT can provide the functional information and therefore can be used to trace the pathological and physiological processes at the molecular level. Further, FMT can be used to quantify expression of tumor proteins for cancer assessment and treatment [3–11].

Since optical tomography remains a challenge, researchers have proposed many different methods [12]. Images of FMT are reconstructed based on the region methods [13, 14]. To tackle the ill-posedness of inverse problem, *A priori* sparsity is introduced [15]. L1-norm regularization is used and the over-relaxation algorithm is improved [16]. To achieve higher image clarity, a shape-based method based on the cosinoidal level set is conceived [17]. In [18], an AI-driven tomography reconstruction approach is proposed to improve the efficiency for the optical tomography system. A computational segmentation approach with statistical inference is developed to identify the cell nucleus [19]. A deep neural network is designed for reconstruction of red blood cells [20]. A fast holographic measurement system with high resolution is presented [21]. A meshless approach is proposed based on the compactly supported basis functions [22]. A wavelet-based method is proposed for FMT, where the principal component analysis is used for solving the inverse problem [23].

Generally, reconstruction for FMT involves the forward and the inverse problems [24]. The first-order sensitivity matrix as Jacobian matrix is commonly used to solve the inverse problem. Actually, the second-order derivatives as the Hessian matrix for iterative reconstruction can help improve the performance of convergence and increase the accuracy of image reconstruction [25]. Therefore, we incorporate the Hessian matrix into the process of reconstruction for FMT. Actually, solving large-scale matrix equation is involved in the inverse problem of FMT. In this paper, the size of the Hessian matrix is reduced. Consequently, the Hessian of reduced size can help speed up solving the matrix equation involved in the inverse problem, and hence can accelerate the reconstruction process. In the section of Appendix, we prove that the columns and the rows of the Hessian can be removed in the iterative reconstruction. Hence, we can simplify the Hessian matrix by removing the columns and the rows. Additionally, the reconstructed results can be affected by the location or number of measurements. To further improve the reconstruction quality, the reconstruction for FMT is implemented based on a strategy of detectors rotation. The whole reconstruction is implemented using measurements taken from the detectors

* Corresponding author: zouwei@suda.edu.cn

of different rotation angles. Measurements from the detectors with more angles are capable to offer more reconstruction information than those with the fix angles. Hence, the quality of reconstruction can be improved. Results demonstrate that the proposed method can significantly speed up the reconstruction process and improve the reconstruction quality.

2 Methods

2.1 Forward problem

For forward problem of FMT, the measurements are predicted according to the distributions of excitation light source and the optical parameters of the objects. The mathematical formulation of the forward problem is described primarily by the Maxwell's equations. The radiative transfer equation (RTE) can be utilized to model the light propagation in tissues [26]. Further, the diffusion equation can be commonly employed to describe the light transportation due to the fact that the RTE involves a large amount of computation [27]. Two partial differential equations are usually employed for FMT to depict the light propagation. They are formulated by

$$(-\nabla \cdot D_e \nabla + k_e)\Phi_e = S_e \tag{1}$$

$$(-\nabla \cdot D_m \nabla + k_m)\Phi_m = \beta \Phi_e \tag{2}$$

Equation (1) models the excitation light propagation. Equation (2) depicts the propagation for the fluorescent light. In equations (1) and (2), ∇ denotes the gradient operator. S_e represents the source of excitation light. $\Phi_{e,m}$ denotes the photon fluence. Subscripts e and m represent the parameters at the excitation and the fluorescent wavelength. The diffusion coefficients $D_{e,m}$ can be defined as

$$\begin{cases} D_e = \dfrac{1}{3\left(\mu_{aei} + \mu_{aef} + \mu'_{se}\right)} \\ D_m = \dfrac{1}{3\left(\mu_{ami} + \mu_{amf} + \mu'_{sm}\right)} \end{cases} \tag{3}$$

The decay coefficients $k_{e,m}$ are defined by

$$\begin{cases} k_e = \dfrac{i\omega}{c} + \mu_{aei} + \mu_{aef} \\ k_m = \dfrac{i\omega}{c} + \mu_{ami} + \mu_{amf} \end{cases} \tag{4}$$

The emission source coefficient β is obtained by

$$\beta = \frac{\eta \mu_{aef}}{1 - i\omega\tau} \tag{5}$$

where μ_{aei} and μ_{ami} stand for the absorption coefficients of non-fluorescing chromophore. μ_{aef} and μ_{amf} denote the absorption coefficients of fluorophore. μ'_{se} and μ'_{sm} represent reduced scattering coefficients. The fluorescence quantum efficiency is denoted by η. τ represents the fluorescent lifetime. c represents the speed of light $i = (-1)^{1/2}$.

In order to obtain the photon fluence, the Robin boundary conditions can be applied for describing the propagation of light on the tissue boundary

$$\mathbf{n} \cdot (D_e \nabla \Phi_e) + b_e \Phi_e = 0 \tag{6}$$

$$\mathbf{n} \cdot (D_m \nabla \Phi_m) + b_m \Phi_m = 0 \tag{7}$$

where $\mathbf{n}$ represents the outer normal of the boundary. b_e and b_m denote the Robin boundary coefficients.

In the framework of the finite element method (FEM) [28–30], the domain Ω can be discretized consisting of P elements and N vertices. Thus, the forward problem can be rewritten as

$$\mathbf{A}_e \Phi_e = \mathbf{S}_e \tag{8}$$

$$\mathbf{A}_m \Phi_m = \mathbf{S}_m \tag{9}$$

where $\mathbf{A}_{e,m}$ can be obtained by

$$a_{\Omega_h}\left(u_i, u_j\right)_{e,m} = \iint_{\Omega_h} D_{e,m} \nabla u_i \cdot \nabla u_j d\Omega + \iint_{\Omega_h} k_{e,m} u_i u_j d\Omega + \int_{\Gamma_h} b_{e,m} u_i u_j \mathrm{d}s \tag{10}$$

Here, Ω_h denotes the domain. Γ_h denotes the boundary. u_i $(i = 1, ..., N)$ represent basis functions.

2.2 Inverse problem

Generally, the linear approximation is commonly used in conventional FMT reconstruction methods. Due to the high computational complexity of the higher-order derivatives involved in the iterative reconstruction, they are neglected in the large-scale reconstruction [31, 32]. Actually, incorporating the Hessian matrix into the process of reconstruction for FMT can help improve the performance of convergence and increase the accuracy of image reconstruction.

In order to derive the framework for the inverse problem based on the Hessian matrix, the inverse reconstruction is formulated as follows

$$M(\mathbf{x}) = \|F(\mathbf{x}) - \mathbf{y}\| \tag{11}$$

Herein, $M(\mathbf{x})$ denotes an objective function. $\mathbf{y} \in \mathbb{R}^M$ represents the measurement. F represents the forward operator and $\mathbf{x} \in \mathbb{R}^N$ stands for the optical parameters.

The above objective function can be expanded in a Taylor series with the first-order term and second-order term

$$M(\mathbf{x} + \Delta\mathbf{x}) = M(\mathbf{x}) + [\nabla M(\mathbf{x})]^T \Delta\mathbf{x} + \frac{1}{2}\Delta\mathbf{x}^T \mathbf{H} \Delta\mathbf{x} \tag{12}$$

Herein, $\Delta\mathbf{x}$ stands for the perturbation in optical parameters, $\nabla M(\mathbf{x})$ stands for the gradient of the objective function at $\mathbf{x}$

$$\nabla M(\mathbf{x}) = \left[\frac{\partial M(\mathbf{x})}{\partial x_1}\frac{\partial M(\mathbf{x})}{\partial x_2}\cdots\frac{\partial M(\mathbf{x})}{\partial x_N}\right]^T \tag{13}$$

As the second-order sensitivity matrix, the Hessian matrix $\mathbf{H}$ represents the second-order partial derivative of M with respect to $\mathbf{x}$. The $N \times N$ Hessian matrix can be achieved by:

$$\mathbf{H} = \begin{bmatrix} \frac{\partial^2 M}{\partial x_1^2} & \frac{\partial^2 M}{\partial x_1 \partial x_2} & \cdots & \frac{\partial^2 M}{\partial x_1 \partial x_N} \\ \frac{\partial^2 M}{\partial x_2 \partial x_1} & \frac{\partial^2 M}{\partial x_2^2} & \cdots & \frac{\partial^2 M}{\partial x_2 \partial x_N} \\ \vdots & \vdots & \ddots & \vdots \\ \frac{\partial^2 M}{\partial x_N \partial x_1} & \frac{\partial^2 M}{\partial x_N \partial x_2} & \cdots & \frac{\partial^2 M}{\partial x_N^2} \end{bmatrix} \tag{14}$$

In order to tackle the ill-posedness of inverse problem for FMT, the regularization parameter λ is introduced [30]. Suppose M attains its extremum at $\mathbf{x} + \mathbf{\Delta x}$, and thus the inverse reconstruction based on the Hessian matrix can be expressed by:

$$\left(\mathbf{H}^T\mathbf{H} + \lambda\mathbf{I}\right)\Delta\mathbf{x} = -\mathbf{H}^T\nabla M(\mathbf{x}) \tag{15}$$

From equation (15), it can be seen that solving matrix equation is involved in the inverse problem. One of the major challenges in the reconstruction is its high computational complexity resulted from larger-scale matrix manipulations. If the size of Hessian is reduced, computation requirements of solving the matrix equation will be reduced. Consequently, the reconstruction process can be accelerated.

2.3 Reduction of the Hessian matrix

During the process of iterative reconstruction of equation (15), the Hessian matrix $\mathbf{H}$ needs to be repeatedly calculated. Thus, the Hessian matrix is critically important for the reconstruction speed. Traditionally, the Hessian matrix can be achieved by direct derivation method, which is computationally expensive especially for large-scale matrices. Hence, it is important to design a calculation method of Hessian matrix for fast reconstruction of FMT. Actually, if the Hessian matrix is simplified, the computing efficiency for inverse reconstruction can be enhanced.

In this paper, we can prove the column $\mathbf{H}_i$ of the Hessian is capable to be removed in the iterative reconstruction of solving equation (15) as $\mathbf{H}_i$ approaches 0 as in the section of Appendix A(1). Therefore, we can simplify the Hessian matrix by removing the columns. Consequently, the computation time for inverse reconstruction can be accelerated. The Hessian matrix is reduced through removing the jth column when the condition as below is satisfied

$$\sum_{i=1}^{N}\left|H_{ij}\right| < \delta \tag{16}$$

where H_{ij} represents the element of the Hessian matrix, and δ denotes a threshold.

Furthermore, we can also prove the row R_i in the Hessian is capable to be removed during the iterative reconstruction when R_i approaches 0 as in the section of Appendix A(2). Thus, the rows in the Hessian matrix are also be removed to further improve the computation efficiency of reconstruction when the following condition is satisfied,

$$\sum_{j=1}^{N}\left|H_{ij}\right| < \delta \tag{17}$$

From equation (A14), it can be seen that the ith row in the Hessian is related to the ith component in $\nabla M(\mathbf{x})$. Therefore, removing the ith row in the Hessian means the ith element in $\nabla M(\mathbf{x})$ can be removed. Consequently, the product of $\mathbf{H}^T\nabla M(\mathbf{x})$ is achieved. Thus, $\nabla M(\mathbf{x})$ is reduced with the reduction of rows in the Hessian. With the reduction of Hessian, solving the matrix equation involved in the inverse problem as in equation (15) can be accelerated, which is beneficial for speeding up the reconstruction process. Therefore, the computational complexity of inverse reconstruction is reduced.

2.4 Reconstruction with the strategy of detectors rotation

Basically, the detectors are placed at the fixed positions in inverse reconstruction. The location or number of measurements can also affect the reconstructed results. In order to enhance the reconstruction efficiency, an approach of detectors rotation is combined into the reconstruction. In this approach, the measurements taken from the original detectors are used for reconstruction in the first iteration. Then the measurements taken from the rotated detectors with a certain angle are used for next iteration. The whole reconstruction is implemented using measurements taken from the detectors of different rotation angles. During the process of reconstruction, measurements taken from the detectors with more angles are capable to offer more reconstruction information than those with the fix angles. Hence, the quality of reconstruction can be improved. In this paper, we set the rotation angle as a half of the angle between the adjacent detectors. Figure 1 depicts the strategy of detectors rotation.

3 Results and discussion

To validate the proposed method, we first use the simulated phantom with one inclusion as shown in Figure 2 to test the performance. The simulated input data is used to assess the performance of the algorithm. Four excitation light sources and fifteen detectors are evenly placed around of the phantom, where the triangle denotes the excitation light source and the circle denotes the detector. The inverse reconstruction is performed with the grid containing 212 triangular elements as shown in Figure 3 [23].

Table 1 lists the details for optical parameters of the reconstruction phantom. To quantitatively evaluate the reconstruction results, the mean square error (MSE) is introduced

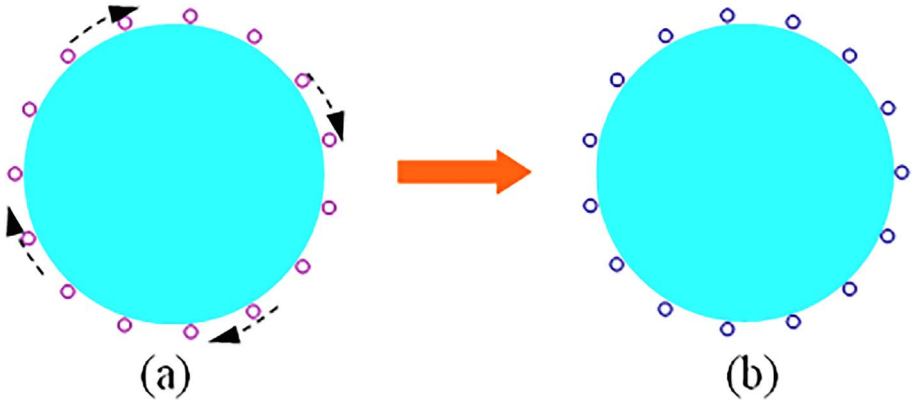

Figure 1. Illustration of the approach of detectors rotation. (a) Detectors before the rotation. (b) Detectors after the rotation.

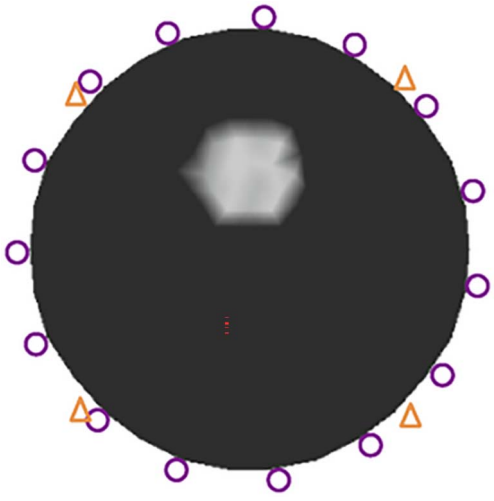

Figure 2. Simulated phantom of one inclusion.

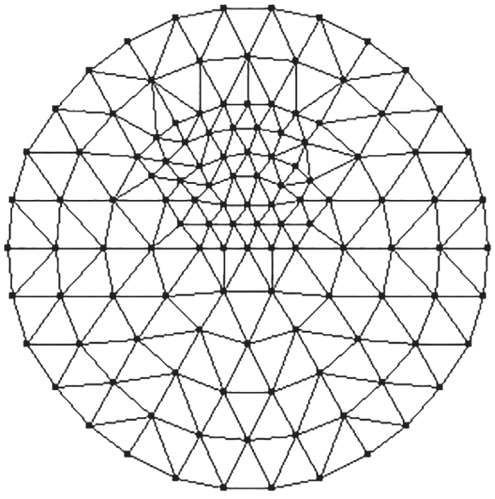

Figure 3. Reconstruction grid for one inclusion.

Table 1. Optical parameters for one-inclusion phantom.

Excitation light	$\mu_{aef}(\text{mm})^{-1}$	$\mu_{aei}(\text{mm})^{-1}$	$\mu'_{se}(\text{mm}^{-1})$	$\tau(ns)$	η
Inclusion	0.4	0.03	0.2	0.5	0.16
Background	0.05	0.03	0.2	0.5	0.16
Fluorescent light	$\mu_{amf}(\text{mm})^{-1}$	$\mu_{ami}(\text{mm})^{-1}$	$\mu'_{sm}(\text{mm}^{-1})$	$\tau(ns)$	η
Inclusion	0.04	0.02	0.1	0.5	0.16
Background	0.006	0.02	0.1	0.5	0.16

$$\text{MSE} = \frac{1}{N}\sum_{i=1}^{N}[x^{rea}(i) - x^{rec}(i)]^2 \tag{18}$$

where the superscript *rea* stands for the real values of the optical parameters and *rec* stands for the reconstructed optical parameters. To choose the threshold δ, another parameter is introduced as

$$\delta = \epsilon \times \sum_{j=1}^{N}\sum_{i=1}^{N}\left|H_{ij}\right| \tag{19}$$

where $\in$ is set as 0.05 in this work.

The reconstructed results of μ_{aef} of one-inclusion phantom using the proposed approach and that using the Jacobian matrix are depicted in Figure 4(a) and 4(b), respectively. We see the proposed method yields the reconstruction result with improved quality comparatively to the method based on the Jacobian matrix. Table 2 lists the performance of reconstructions in terms of the computational time and MSE for quantitative validation. The reconstructions are implemented based on the computer with CPU at

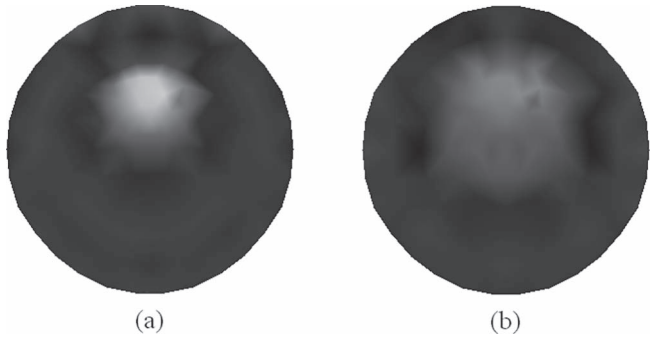

Figure 4. Reconstructed results of absorption coefficient μ_{aef} of one-inclusion phantom. (a) Reconstructed result using the proposed approach. (b) Reconstructed result using the Jacobian matrix.

Table 2. Method performance of phantom of one inclusion.

Methods	Method using the Jacobian matrix	Proposed approach
Computational time (s)	207	147
MSE	4.952×10^{-4}	2.734×10^{-4}

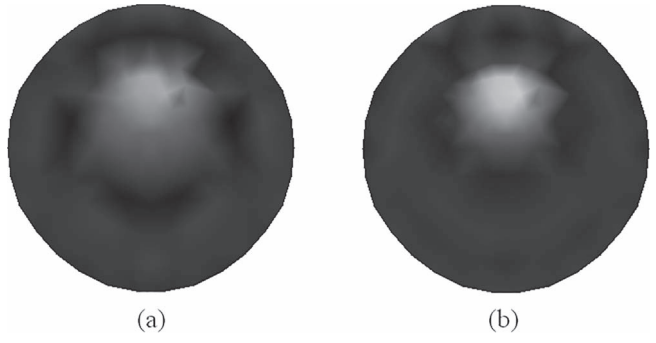

Figure 5. Reconstructed results of absorption coefficient of one-inclusion phantom. (a) Reconstructed result without the strategy of detectors rotation. (b) Reconstructed result using the proposed approach.

2.6 GHz and 1 GB RAM. We remark the computational time of the proposed approach is faster than that of the Jacobian matrix method. Additionally, the MSE of our approach is smaller than that of the Jacobian matrix method. Therefore, the proposed method accelerates the inverse reconstruction process and achieves high precision.

To validate the performance of the strategy of detectors rotation, Figure 5(a) and 5(b) provide the results without the strategy of detectors rotation and that with the proposed method, respectively. Table 3 provides the quantitative comparisons of different reconstructions. It is observed that the approach of detectors rotation improves the performance for reconstruction.

Figure 6 shows the simulated phantom, which contains two inclusions with different shapes. Four excitation light sources are uniformly located on the boundary of this phantom. The measurements are achieved from fifteen detectors around the phantom. The triangle denotes the excitation light source and the circle denotes the detector. The reconstruction is implemented based on the grid consisting of 264 triangular elements, which is described in Figure 7 [23]. Table 4 lists the values of optical parameters of the phantom.

The reconstructed image using our approach is provided in Figure 8(a) and the result from the method based on the

Table 3. Method performance of phantom of one inclusion.

Methods	Proposed approach	Method without the strategy of detectors rotation
Computational time (s)	147	155
MSE	2.734×10^{-4}	3.967×10^{-4}

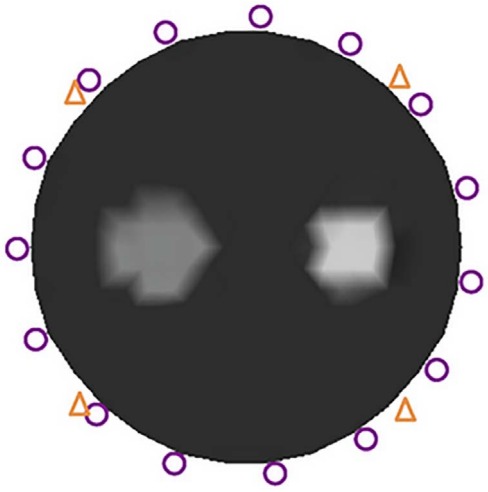

Figure 6. Simulated phantom with two inclusions.

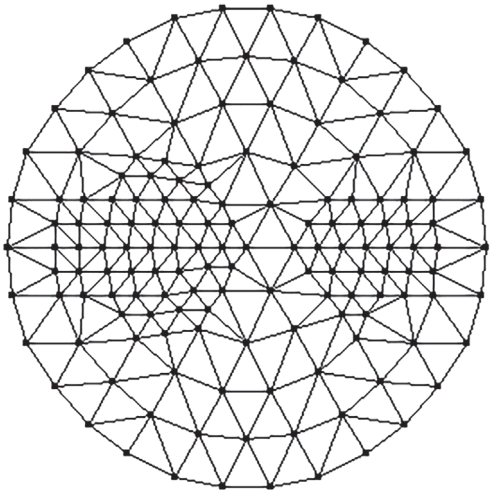

Figure 7. Reconstruction grid for two inclusions.

Table 4. Optical parameters for two-inclusion phantom.

Excitation light	$\mu_{aef}(\text{mm})^{-1}$	$\mu_{aei}(\text{mm})^{-1}$	$\mu'_{se}(\text{mm}^{-1})$	$\tau(ns)$	η
Inclusions	0.3, 0.4	0.03	0.2	0.5	0.16
Background	0.05	0.03	0.2	0.5	0.16
Fluorescent light	$\mu_{amf}(\text{mm})^{-1}$	$\mu_{ami}(\text{mm})^{-1}$	$\mu'_{sm}(\text{mm}^{-1})$	$\tau(ns)$	η
Inclusions	0.03, 0.04	0.02	0.1	0.5	0.16
Background	0.006	0.02	0.1	0.5	0.16

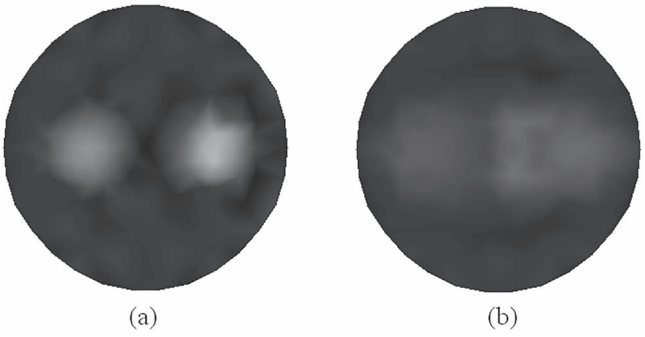

Figure 8. Reconstructed results of absorption coefficient μ_{aef} of two-inclusion phantom. (a) Reconstructed result using the proposed approach. (b) Reconstructed result using the Jacobian matrix.

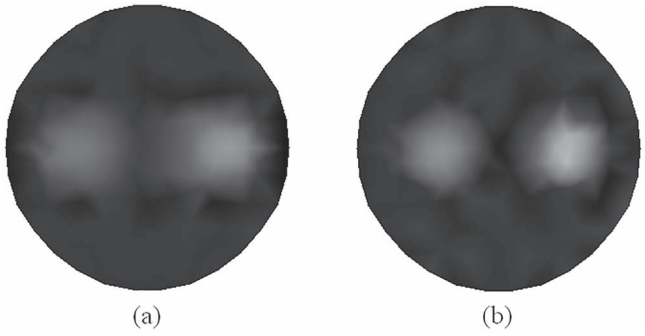

Figure 9. Reconstructed results of absorption coefficient of two-inclusion phantom. (a) Reconstructed result without the strategy of detectors rotation. (b) Reconstructed image using the proposed approach.

Table 5. Method performance of phantom of two inclusions.

Methods	Method using the Jacobian matrix	Proposed approach
Computational time (s)	293	220
MSE	5.301×10^{-4}	3.495×10^{-4}

Table 6. Method performance of phantom of two inclusions.

Methods	Proposed approach	Method without the strategy of detectors rotation
Computational time (s)	220	236
MSE	3.495×10^{-4}	4.578×10^{-4}

Jacobian matrix is given in Figure 8(b). We see the quality of image can be enhanced by our method. Table 5 presents the quantitative comparisons of different reconstruction methods. It can be seen that the improvement in reconstruction accuracy is achieved using the proposed approach. In addition, we can see that the computational time of the proposed approach is less than that using the Jacobian matrix method. Thus, our approach improves the computation efficiency with high quality.

The reconstruction result without the approach of detectors rotation and that with the proposed approach are described in Figure 9(a) and 9(b). The performance of reconstruction from different methods is described in Table 6. We can observe that improvements in reconstruction quality are gained with the strategy of detectors rotation.

In order to investigate the effect of reducing the size of Hessian matrix, reconstructions based on the proposed method and without reduction of the Hessian matrix are performed. The comparison of performance is listed in

Table 7. Comparison of performance for phantom of two inclusions.

Methods	Method without reduction of the Hessian matrix	Proposed approach
Computational time (s)	265	220
MSE	3.374×10^{-4}	3.495×10^{-4}

Table 8. Comparison of performance for phantom of two inclusions.

Methods	Proposed approach	Method using the Jacobian matrix
Computational time (s)	220	293
MSE	3.876×10^{-4}	6.121×10^{-4}

Table 7. It can be seen that the method of reduction of Hessian matrix can significantly speed up the reconstruction process at the expense of a small reduction in reconstruction accuracy.

To further evaluate the robustness of the algorithms, Gaussian noise with a signal-to-noise ratio of 10 dB is added to the simulated data. Table 8 shows the reconstruction performance of different reconstruction methods. It can be seen that our approach is able to achieve the reconstruction results with high quality.

4 Conclusions

In this paper, an efficient method for image reconstruction of FMT based on the reduction of Hessian matrix is developed. Further, the strategy of detectors rotation is combined into the inverse reconstruction to enhance the quality of reconstruction. We see from the reconstruction results that the proposed method can considerably accelerate the reconstruction of FMT. In addition, the proposed method improves the accuracy for the inverse solutions.

Funding

This work was supported by Suzhou Science and Technology Planning Project (Grant No. SKJY2021044), Natural Science Foundation of Jiangsu Province, China (Grant No. BK20130324, BK20171249), Specialized Research Fund for the Doctoral Program of Higher Education (SRFDP) (Grant No. 20123201120009), and Natural Science Foundation of the Jiangsu Higher Education Institutions of China (Grant No. 12KJB510029).

Conflicts of interest

The authors declare that they have no conflict of interest.

Data availability statement

The datasets generated during the current study are available from the corresponding author on reasonable request.

Author contribution statement

Conceptualization, W.Z.; methodology, W.Z and J.W.; software, W.Z.; validation, W.Z. and J.W.; formal analysis, W.Z. and J.W.; writing—original draft preparation, W.Z.; writing—review and editing, W.Z; supervision, J.W.

References

1 Balas C. (2009) Review of biomedical optical imaging—a powerful, non-invasive, non-ionizing technology for improving in vivo diagnosis, *Meas. Sci. Technol.* **20**, 1–12.
2 Darne C., Lu Y., Sevick-Muraca E.M. (2014) Small animal fluorescence and bioluminescence tomography: a review of approaches, algorithms and technology update, *Phys. Med. Biol.* **59**, R1–R64.
3 Ntziachristos V. (2006) Fluorescence molecular imaging, *Annu. Rev. Biomed. Eng.* **8**, 1–33.
4 Zhang J., Shi J., Guang H., Zuo S., Liu F., Bai J., Luo J. (2016) Iterative correction scheme based on discrete cosine transform and L1 regularization for fluorescence molecular tomography with background fluorescence, *IEEE Trans. Biomed. Eng.* **63**, 1107–1115.
5 Mozumder M., Tarvainen T., Arridge S., Kaipio J.P., D'Andrea C., Kolehmainen V. (2016) Approximate marginalization of absorption and scattering in fluorescence diffuse optical tomography, *Inverse Probl. Imag.* **10**, 227–246.
6 Jiang S., Liu J., An Y., Gao Y., Meng H., Wang K., Tian J. (2020) Fluorescence molecular tomography based on group sparsity priori for morphological reconstruction of glioma, *IEEE Trans. Biomed. Eng.* **67**, 1429–1437.
7 Lian L., Deng Y., Xie W., Xu G., Yang X., Zhang Z., Luo Q. (2017) Enhancement of the localization and quantitative performance of fluorescence molecular tomography by using linear nBorn method, *Opt. Express* **25**, 2063–2079.
8 Wang B., Zhang Y., Liu D., Ding X., Dan M., Pan T., Zhao H., Gao F. (2019) Sparsity-regularized approaches to directly reconstructing hemodynamic response in brain functional diffuse optical tomography, *Appl. Opt.* **58**, 863–870.
9 Cong A., Cong W.X., Lu Y.J., Santago P., Chatziioannou A., Wang G. (2010) Differential evolution approach for regularized bioluminescence tomography, *IEEE Trans. Biomed. Eng.* **57**, 2229–2238.
10 Mohajerani P., Ntziachristos V. (2016) Inversion scheme for hybrid fluorescence molecular tomography using a fuzzy inference system, *IEEE Trans. Med. Imaging* **35**, 381–390.
11 Kwong T.C., Nouizi F., Lin Y., Cho J., Zhu Y., Sampathkumaran U., Gulsen G. (2017) Experimental evaluation of the resolution and quantitative accuracy of temperature-modulated fluorescence tomography, *Appl. Opt.* **56**, 521–529.
12 An Y., Wang K., Tian J. (2018) Recent methodology advances in fluorescence molecular tomography, *Vis. Comput. Ind. Biomed. Art* **1**, 1–11.
13 Zou W., Wang J., Feng D.D. (2010) Region-based reconstruction method for fluorescent molecular tomography, *J. Opt. Soc. Am. A* **27**, 2327–2336.
14 An Y., Liu J., Zhang G., Ye J., Du Y., Mao Y., Chi C., Tian J. (2015) A novel region reconstruction method for fluorescence molecular tomography, *IEEE Trans. Biomed. Eng.* **62**, 1818–1826.
15 Wang B., Zhang Y., Liu D., Ding X., Dan M., Pan T., Zhao H., Gao F. (2019) Sparsity-regularized approaches to directly reconstructing hemodynamic response in brain functional diffuse optical tomography, *Appl. Opt.* **58**, 863–870.
16 Fang E., Wang J., Hu D., Zhang J., Zou W., Zhou Y. (2015) Adaptive monotone fast iterative shrinkage thresholding algorithm for fluorescence molecular tomography, *IET Sci. Meas. Technol.* **9**, 587–595.
17 Zhang X., Cao X., Zhu S. (2017) Reconstruction of fluorescence molecular tomography with a cosinoidal level set method, *BioMed. Eng.* **16**, 1–17.
18 Sun J., Yang B., Koukourakis N., Guck J., Czarske Juergen W. (2024) AI-driven projection tomography with multicore fibre-optic cell rotation, *Nat. Commun.* **15**, 1–11.
19 Pirone D., Lim J., Merola F., et al. (2022) Stain-free identification of cell nuclei using tomographic phase microscopy in flow cytometry, *Nat. Photon.* **16**, 851–859.
20 Joowon L., Ahmed B.A., Demetri P. (2020) Three-dimensional tomography of red blood cells using deep learning, *Adv. Photon.* **2**, 1–9.
21 Ramos Ruiz A.E., Gürtler J., Kuschmierz R., Czarske J.W. (2019) Measurement of the local sound pressure on a bias-flow liner using high-speed holography and tomographic reconstruction, *IEEE Access* **7**, 153466–153474.

22 An Y., Liu J., Zhang G., Ye J., Mao Y., Jiang S., Shang W., Du Y., Chi C., Tian J. (2015) Meshless reconstruction method for fluorescence molecular tomography based on compactly supported radial basis function, *J. Biomed. Opt.* **20**, 1–11.
23 Zou W., Wang J., Hu D., Wang W. (2015) A reconstruction approach in wavelet domain for fluorescent molecular tomography via rotated sources illumination, *BiomMed. Eng. OnLine* **14**, 1–18.
24 Arridge S.R., Schotland J.C. (2009) Optical tomography: forward and inverse problems, *Inverse Probl.* **25**, 1–59.
25 Biswas S.K., Kanhirodan R., Vasu R.M., Roy D. (2012) Practical fully three-dimensional reconstruction algorithms for diffuse optical tomography, *J. Opt. Soc. Am. A* **29**, 1017–1026.
26 Klose A.D. (2009) *Radiative transfer of luminescence light in biological tissue, light scattering reviews 4: Single light scattering and radiative transfer*, Springer, Berlin Heidelberg.
27 Hayashi T., Kashio Y., Okada E. (2003) Hybrid Monte Carlo–diffusion method for light propagation in tissue with a low-scattering region, *Appl. Opt.* **42**, 2888–2896.
28 Joshi A., Bangerth W., Sevick-Muraca E.M. (2004) Adaptive finite element based tomography for fluorescence optical imaging in tissue, *Opt. Express* **12**, 5402–5417.
29 Arridge S.R., Hebden J.C. (1997) Optical imaging in medicine: II. Modelling and reconstruction, *Phys. Med. Biol.* **42**, 841–853.
30 Arridge S.R. (1999) Optical tomography in medical imaging, *Inverse Prob.* **15**, R41–R49.
31 Arridge S.R., Schweiger M. (1998) A general framework for iterative reconstruction algorithms in optical tomography using a finite element method, in:*Computational radiology and imaging: therapy and diagnosis. IMA volumes in mathematics and its applications*, Springer.
32 Gibson A.P., Hebden J.C., Arridge S.R. (2005) Recent advances in diffuse optical imaging, *Phys. Med. Biol.* **50**, R1–R43.

Appendix A

1. Proof.

Let

$$\Delta\mathbf{x} = (\,\Delta x_1 \quad \Delta x_2 \quad \cdots \quad \Delta x_i \quad \cdots \quad \Delta x_N\,)^T \quad \left(\Delta\mathbf{x} \in \mathbb{R}^N\right)$$

and

$$\mathbf{H} = (\,H_1 \quad H_2 \quad \cdots \quad H_i \quad \cdots \quad H_N\,) \quad \left(\mathbf{H} \in \mathbb{R}^{N\times N}\right)$$

stand for the perturbation of optical parameters and the Hessian, which are substituted into equation (15). Then, we can obtain

$$\left[\begin{pmatrix} H_1^T \\ H_2^T \\ \vdots \\ H_i^T \\ \vdots \\ H_N^T \end{pmatrix} \cdot (\,H_1 \quad H_2 \quad \cdots \quad H_i \quad \cdots \quad H_N\,) + \lambda\mathbf{I}\right] \cdot \begin{pmatrix} \Delta x_1 \\ \Delta x_2 \\ \vdots \\ \Delta x_i \\ \vdots \\ \Delta x_N \end{pmatrix} = -\begin{pmatrix} H_1^T \\ H_2^T \\ \vdots \\ H_i^T \\ \vdots \\ H_N^T \end{pmatrix} \cdot \nabla M(\mathbf{x}) \tag{A1}$$

Equation (A1) can be written as follows

$$\begin{pmatrix} H_1^TH_1+\lambda & H_1^TH_2 & \cdots & H_1^TH_i & \cdots & H_1^TH_N \\ H_2^TH_1 & H_2^TH_2+\lambda & \cdots & H_2^TH_i & \cdots & H_2^TH_N \\ \vdots & \vdots & \ddots & \vdots & & \vdots \\ H_i^TH_1 & H_i^TH_2 & \cdots & H_i^TH_i+\lambda & \cdots & H_i^TH_N \\ \vdots & \vdots & & \vdots & \ddots & \vdots \\ H_N^TH_1 & H_N^TH_2 & \cdots & H_N^TH_i & \cdots & H_N^TH_N+\lambda \end{pmatrix} \cdot \begin{pmatrix} \Delta x_1 \\ \Delta x_2 \\ \vdots \\ \Delta x_i \\ \vdots \\ \Delta x_N \end{pmatrix} = -\begin{pmatrix} H_1^T\cdot\nabla M(\mathbf{x}) \\ H_2^T\cdot\nabla M(\mathbf{x}) \\ \vdots \\ H_i^T\cdot\nabla M(\mathbf{x}) \\ \vdots \\ H_N^T\cdot\nabla M(\mathbf{x}) \end{pmatrix} \tag{A2}$$

From equation (A2), the ith equation can be formulated by

$$\left(H_i^TH_1 \quad H_i^TH_2 \quad \cdots \quad H_i^TH_i+\lambda \quad \cdots \quad H_i^TH_N\right)\cdot\Delta\mathbf{x} = -H_i^T\cdot\nabla M(\mathbf{x}) \tag{A3}$$

Then,

$$\Delta x_i = \frac{-H_i^T(\nabla M(\mathbf{x}) + \Delta x_1 H_1 + \Delta x_2 H_2 \cdots + \Delta x_{i-1} H_{i-1} + \Delta x_{i+1} H_{i+1} \cdots + \Delta x_N H_N)}{H_i^T H_i + \lambda} \tag{A4}$$

The limit of Δx_i as H_i tends towards 0 is obtained by

$$\lim_{H_i \to 0} \Delta x_i = \lim_{H_i \to 0} \frac{-H_i^T(\nabla M(\mathbf{x}) + \Delta x_1 H_1 + \Delta x_2 H_2 \cdots + \Delta x_{i-1} H_{i-1} + \Delta x_{i+1} H_{i+1} \cdots + \Delta x_N H_N)}{H_i^T H_i + \lambda} = 0 \tag{A5}$$

Equation (A1) can be rewritten as follows

$$\begin{pmatrix} H_1^T \mathbf{H}\Delta\mathbf{x} \\ H_2^T \mathbf{H}\Delta\mathbf{x} \\ \vdots \\ H_i^T \mathbf{H}\Delta\mathbf{x} \\ \vdots \\ H_N^T \mathbf{H}\Delta\mathbf{x} \end{pmatrix} + \lambda\mathbf{I} \cdot \begin{pmatrix} \Delta x_1 \\ \Delta x_2 \\ \vdots \\ \Delta x_i \\ \vdots \\ \Delta x_N \end{pmatrix} = - \begin{pmatrix} H_1^T \nabla M(\mathbf{x}) \\ H_2^T \nabla M(\mathbf{x}) \\ \vdots \\ H_i^T \nabla M(\mathbf{x}) \\ \vdots \\ H_N^T \nabla M(\mathbf{x}) \end{pmatrix} \tag{A6}$$

When H_i approaches 0, we have

$$\lim_{H_i \to 0} \left[\begin{pmatrix} H_1^T \mathbf{H}\Delta\mathbf{x} \\ H_2^T \mathbf{H}\Delta\mathbf{x} \\ \vdots \\ H_i^T \mathbf{H}\Delta\mathbf{x} \\ \vdots \\ H_N^T \mathbf{H}\Delta\mathbf{x} \end{pmatrix} + \lambda\mathbf{I} \cdot \begin{pmatrix} \Delta x_1 \\ \Delta x_2 \\ \vdots \\ \Delta x_i \\ \vdots \\ \Delta x_N \end{pmatrix} \right] = - \lim_{H_i \to 0} \begin{pmatrix} H_1^T \nabla M(\mathbf{x}) \\ H_2^T \nabla M(\mathbf{x}) \\ \vdots \\ H_i^T \nabla M(\mathbf{x}) \\ \vdots \\ H_N^T \nabla M(\mathbf{x}) \end{pmatrix} \tag{A7}$$

Because $\lim_{H_i \to 0} H_i^T \mathbf{H}\Delta\mathbf{x} = 0$, $\lim_{H_i \to 0} \Delta x_i = 0$ and $\lim_{H_i \to 0} H_i^T \nabla M(\mathbf{x}) = 0$, we have

$$\lim_{H_i \to 0} \left[\begin{pmatrix} H_1^T \mathbf{H}\Delta\mathbf{x} \\ H_2^T \mathbf{H}\Delta\mathbf{x} \\ \vdots \\ H_{i-1}^T \mathbf{H}\Delta\mathbf{x} \\ 0 \\ H_{i+1}^T \mathbf{H}\Delta\mathbf{x} \\ \vdots \\ H_N^T \mathbf{H}\Delta\mathbf{x} \end{pmatrix} + \lambda\mathbf{I} \cdot \begin{pmatrix} \Delta x_1 \\ \Delta x_2 \\ \vdots \\ \Delta x_{i-1} \\ 0 \\ \Delta x_{i+1} \\ \vdots \\ \Delta x_N \end{pmatrix} \right] = - \lim_{H_i \to 0} \begin{pmatrix} H_1^T \nabla M(\mathbf{x}) \\ H_2^T \nabla M(\mathbf{x}) \\ \vdots \\ H_{i-1}^T \nabla M(\mathbf{x}) \\ 0 \\ H_{i+1}^T \nabla M(\mathbf{x}) \\ \vdots \\ H_N^T \nabla M(\mathbf{x}) \end{pmatrix} \tag{A8}$$

Then, we have

$$\lim_{H_i\to 0}\left[\begin{pmatrix} H_1^T\mathbf{H}\Delta\mathbf{x} \\ H_2^T\mathbf{H}\Delta\mathbf{x} \\ \vdots \\ H_{i-1}^T\mathbf{H}\Delta\mathbf{x} \\ H_{i+1}^T\mathbf{H}\Delta\mathbf{x} \\ \vdots \\ H_N^T\mathbf{H}\Delta\mathbf{x} \end{pmatrix} + \lambda\mathbf{I}\cdot\begin{pmatrix} \Delta x_1 \\ \Delta x_2 \\ \vdots \\ \Delta x_{i-1} \\ \Delta x_{i+1} \\ \vdots \\ \Delta x_N \end{pmatrix}\right] = -\lim_{H_i\to 0}\begin{pmatrix} H_1^T\nabla M(\mathbf{x}) \\ H_2^T\nabla M(\mathbf{x}) \\ \vdots \\ H_{i-1}^T\nabla M(\mathbf{x}) \\ H_{i+1}^T\nabla M(\mathbf{x}) \\ \vdots \\ H_N^T\nabla M(\mathbf{x}) \end{pmatrix} \tag{A9}$$

Equation (A9) can be rewritten by

$$\lim_{H_i\to 0}\left[\begin{pmatrix} H_1^T \\ H_2^T \\ \vdots \\ H_{i-1}^T \\ H_{i+1}^T \\ \vdots \\ H_N^T \end{pmatrix}\cdot(H_1\Delta x_1 + H_2\Delta x_2 + \cdots + H_i\Delta x_i + \cdots H_N\Delta x_N) + \lambda\mathbf{I}\cdot\begin{pmatrix} \Delta x_1 \\ \Delta x_2 \\ \vdots \\ \Delta x_{i-1} \\ \Delta x_{i+1} \\ \vdots \\ \Delta x_N \end{pmatrix}\right] = -\lim_{H_i\to 0}\begin{pmatrix} H_1^T\nabla M(\mathbf{x}) \\ H_2^T\nabla M(\mathbf{x}) \\ \vdots \\ H_{i-1}^T\nabla M(\mathbf{x}) \\ H_{i+1}^T\nabla M(\mathbf{x}) \\ \vdots \\ H_N^T\nabla M(\mathbf{x}) \end{pmatrix} \tag{A10}$$

Because $\lim_{H_i\to 0} H_i\Delta x_i = 0$, we can obtain

$$\lim_{H_i\to 0}\left[\begin{pmatrix} H_1^T \\ H_2^T \\ \vdots \\ H_{i-1}^T \\ H_{i+1}^T \\ \vdots \\ H_N^T \end{pmatrix}\cdot(H_1\Delta x_1 + H_2\Delta x_2 + \cdots + H_{i-1}\Delta x_{i-1} + H_{i+1}\Delta x_{i+1}\cdots H_N\Delta x_N) + \lambda\mathbf{I}\cdot\begin{pmatrix} \Delta x_1 \\ \Delta x_2 \\ \vdots \\ \Delta x_{i-1} \\ \Delta x_{i+1} \\ \vdots \\ \Delta x_N \end{pmatrix}\right] = -\lim_{H_i\to 0}\begin{pmatrix} H_1^T\nabla M(\mathbf{x}) \\ H_2^T\nabla M(\mathbf{x}) \\ \vdots \\ H_{i-1}^T\nabla M(\mathbf{x}) \\ H_{i+1}^T\nabla M(\mathbf{x}) \\ \vdots \\ H_N^T\nabla M(\mathbf{x}) \end{pmatrix} \tag{A11}$$

Then, we have

$$\lim_{H_i\to 0}\left[\begin{pmatrix} H_1^T \\ H_2^T \\ \vdots \\ H_{i-1}^T \\ H_{i+1}^T \\ \vdots \\ H_N^T \end{pmatrix}\cdot(H_1 \quad H_2 \quad \cdots \quad H_{i-1} \quad H_{i+1} \quad \cdots \quad H_N) + \lambda\mathbf{I}\right]\cdot\begin{pmatrix} \Delta x_1 \\ \Delta x_2 \\ \vdots \\ \Delta x_{i-1} \\ \Delta x_{i+1} \\ \vdots \\ \Delta x_N \end{pmatrix} = -\lim_{H_i\to 0}\begin{pmatrix} H_1^T \\ H_2^T \\ \vdots \\ H_{i-1}^T \\ H_{i+1}^T \\ \vdots \\ H_N^T \end{pmatrix}\cdot\nabla M(\mathbf{x}) \tag{A12}$$

From equations (A1) and (A12), we see the ith column H_i in the Hessian is capable to be removed as H_i tends towards 0 for solving equation (15).

2. Proof.

Let

$$\nabla M(\mathbf{x}) = \begin{pmatrix} \nabla M(\mathbf{x})_1 & \nabla M(\mathbf{x})_2 & \cdots & \nabla M(\mathbf{x})_i & \cdots & \nabla M(\mathbf{x})_N \end{pmatrix}^T \quad \left(\nabla M(\mathbf{x}) \in \mathbb{R}^N\right)$$

and

$$\mathbf{H} = \begin{pmatrix} R_1^T & R_2^T & \cdots & R_i^T & \cdots & R_N^T \end{pmatrix}^T \quad \left(\mathbf{H} \in \mathbb{R}^{N\times N}\right)$$

Substituting them into equation (15), we can obtain

$$\left[\begin{pmatrix} R_1^T & R_2^T & \cdots & R_i^T & \cdots & R_N^T \end{pmatrix} \cdot \begin{pmatrix} R_1 \\ R_2 \\ \vdots \\ R_i \\ \vdots \\ R_N \end{pmatrix} + \lambda \mathbf{I}\right] \cdot \nabla \mathbf{x} = -\begin{pmatrix} R_1^T & R_2^T & \cdots & R_i^T & \cdots & R_N^T \end{pmatrix} \cdot \begin{pmatrix} \nabla M(\mathbf{x})_1 \\ \nabla M(\mathbf{x})_2 \\ \vdots \\ \nabla M(\mathbf{x})_i \\ \vdots \\ \nabla M(\mathbf{x})_N \end{pmatrix} \tag{A13}$$

From equation (A13), we have

$$\begin{aligned} &\left[\left(R_1^T R_1 + R_2^T R_2 + \cdots R_i^T R_i + \cdots R_N^T R_N\right) + \lambda \mathbf{I}\right] \cdot \nabla \mathbf{x} \\ &\quad = -\left(\nabla M(\mathbf{x})_1 R_1^T + \nabla M(\mathbf{x})_2 R_2^T + \cdots + \nabla M(\mathbf{x})_i R_i^T + \cdots \nabla M(\mathbf{x})_N R_N^T\right) \end{aligned} \tag{A14}$$

When R_i approaches 0, we have

$$\begin{aligned} \lim_{R_i \to 0} \left[\left(R_1^T R_1 + R_2^T R_2 + \cdots R_i^T R_i + \cdots R_N^T R_N\right) + \lambda \mathbf{I}\right] \cdot \nabla \mathbf{x} = -\lim_{R_i \to 0} \big(\nabla M(\mathbf{x})_1 R_1^T + \nabla M(\mathbf{x})_2 R_2^T + \\ \cdots + \nabla M(\mathbf{x})_i R_i^T + \cdots \nabla M(\mathbf{x})_N R_N^T\big) \end{aligned} \tag{A15}$$

Because $\lim_{R_i \to 0} R_i^T R_i = 0$ and $\lim_{R_i \to 0} \nabla M(\mathbf{x})_i R_i^T = 0$, we have

$$\begin{aligned} &\lim_{R_i \to 0} \left[\left(R_1^T R_1 + R_2^T R_2 + \cdots R_{i-1}^T R_{i-1} + R_{i+1}^T R_{i+1} \cdots R_N^T R_N\right) + \lambda \mathbf{I}\right] \cdot \\ \nabla \mathbf{x} = -\lim_{R_i \to 0} &\left(\nabla M(\mathbf{x})_1 R_1^T + \nabla M(\mathbf{x})_2 R_2^T + \cdots + \nabla M(\mathbf{x})_{i-1} R_{i-1}^T + \nabla M(\mathbf{x})_{i+1} R_{i+1}^T \cdots \nabla M(\mathbf{x})_N R_N^T\right) \end{aligned} \tag{A16}$$

Equation (A16) can be rewritten by

$$\lim_{R_i \to 0} \left[\begin{pmatrix} R_1^T & R_2^T & \cdots & R_{i-1}^T & R_{i+1}^T & \cdots & R_N^T \end{pmatrix} \cdot \begin{pmatrix} R_1 \\ R_2 \\ \vdots \\ R_{i-1} \\ R_{i+1} \\ \vdots \\ R_N \end{pmatrix} + \lambda \mathbf{I}\right] \cdot \Delta \mathbf{x} = -\lim_{R_i \to 0} \cdot \begin{pmatrix} R_1^T & R_2^T & \cdots & R_{i-1}^T & R_{i+1}^T & \cdots & R_N^T \end{pmatrix} \cdot \begin{pmatrix} \nabla M(\mathbf{x})_1 \\ \nabla M(\mathbf{x})_2 \\ \vdots \\ \nabla M(\mathbf{x})_{i-1} \\ \nabla M(\mathbf{x})_{i+1} \\ \vdots \\ \nabla M(\mathbf{x})_N \end{pmatrix} \tag{A17}$$

From equations (A13) and (A17), we see that the ith row R_i in the Hessian is capable to be removed as R_i tends towards 0 for solving equation (15).